01 Jul 2013

Near- and Far-Field Spectroscopic Imaging Investigation of Resonant Square-Loop Infrared Metasurfaces

J. D'Achangel

E. Tucker

Edward C. Kinzel
Missouri University of Science and Technology, kinzele@mst.edu

E. A. Muller

et. al. For a complete list of authors, see https://scholarsmine.mst.edu/mec_aereng_facwork/3729

Recommended Citation

J. D'Achangel et al., "Near- and Far-Field Spectroscopic Imaging Investigation of Resonant Square-Loop Infrared Metasurfaces," *Optics Express*, vol. 21, no. 14, pp. 17150-17160, Optical Society of America, Jul 2013.
The definitive version is available at https://doi.org/10.1364/OE.21.017150

Near- and far-field spectroscopic imaging investigation of resonant square-loop infrared metasurfaces

Jeffrey D' Archangel,[1] Eric Tucker,[2] Ed Kinzel,[3] Eric A. Muller,[4] Hans A. Bechtel,[5] Michael C. Martin,[5] Markus B. Raschke,[4] and Glenn Boreman[2,*]

[1]*CREOL, The College of Optics & Photonics, University of Central Florida, 4000 Central Florida Blvd., Orlando, FL 32816, USA*

[2]*Department of Physics and Optical Science, University of North Carolina at Charlotte, 9201 University City Blvd., Charlotte, NC 28223, USA*

[3]*Department of Mechanical and Aerospace Engineering, Missouri University of Science and Technology, 400 W. 13th St., Rolla, MO 65409, USA*

[4]*Department of Physics, Department of Chemistry, and JILA, University of Colorado, 390 UCB, Boulder, CO 80309, USA*

[5]*Advanced Light Source Division, Lawrence Berkeley National Laboratory, 1 Cyclotron Road, Berkeley, CA 94720, USA*

[*]*gboreman@uncc.edu*

Abstract: Optical metamaterials have unique properties which result from geometric confinement of the optical conductivity. We developed a series of infrared metasurfaces based on an array of metallic square loop antennas. The far-field absorption spectrum can be designed with resonances across the infrared by scaling the geometric dimensions. We measure the amplitude and phase of the resonant mode as standing wave patterns within the square loops using scattering-scanning near-field optical microscopy (*s*-SNOM). Further, using a broad-band synchrotron-based FTIR microscope and *s*-SNOM at the Advanced Light Source, we are able to correlate far-field spectra to near-field modes of the metasurface as the resonance is tuned between samples. The results highlight the importance of multi-modal imaging for the design and characterization of optical metamaterials.

OCIS codes: (260.3910) Metal optics; (260.5740) Resonance; (310.6628) Subwavelength structures; (180.4243) Near-field microscopy; (300.6300) Spectroscopy; (160.3918) Metamaterials.

References and links

1. H. Butt, Q. Dai, N. Lal, T. D. Wilkinson, J. J. Baumberg, and G. A. J. Amaratunga, "Metamaterial filter for the near-visible spectrum," Appl. Phys. Lett. **101**(8), 083106 (2012).
2. X. Li, L. Yang, C. Hu, X. Luo, and M. Hong, "Tunable bandwidth of band-stop filter by metamaterial cell coupling in optical frequency," Opt. Express **19**(6), 5283–5289 (2011).
3. J. Hao, J. Wang, X. Liu, W. J. Padilla, L. Zhou, and M. Qiu, "High performance optical absorber based on a plasmonic metamaterial," Appl. Phys. Lett. **96**(25), 251104 (2010).
4. G. D'Aguanno, N. Mattiucci, A. Alù, C. Argyropoulos, J. V. Foreman, and M. J. Bloemer, "Thermal emission from a metamaterial wire medium slab," Opt. Express **20**(9), 9784–9789 (2012).
5. J. A. Mason, S. Smith, and D. Wasserman, "Strong absorption and selective thermal emission from a midinfrared metamaterial," Appl. Phys. Lett. **98**(24), 241105 (2011).
6. S. Larouche, Y. J. Tsai, T. Tyler, N. M. Jokerst, and D. R. Smith, "Infrared metamaterial phase holograms," Nat. Mater. **11**(5), 450–454 (2012).
7. N. Yu, P. Genevet, M. A. Kats, F. Aieta, J. P. Tetienne, F. Capasso, and Z. Gaburro, "Light propagation with phase discontinuities: generalized laws of reflection and refraction," Science **334**(6054), 333–337 (2011).
8. L. Huang, X. Chen, H. Mühlenbernd, G. Li, B. Bai, Q. Tan, G. Jin, T. Zentgraf, and S. Zhang, "Dispersionless phase discontinuities for controlling light propagation," Nano Lett. **12**(11), 5750–5755 (2012).
9. G. Biener, A. Niv, V. Kleiner, and E. Hasman, "Metallic subwavelength structures for a broadband infrared absorption control," Opt. Lett. **32**(8), 994–996 (2007).

#188776 - $15.00 USD Received 16 Apr 2013; revised 2 Jul 2013; accepted 4 Jul 2013; published 11 Jul 2013

10. X. Liu, T. Tyler, T. Starr, A. F. Starr, N. M. Jokerst, and W. J. Padilla, "Taming the blackbody with infrared metamaterials as selective thermal emitters," Phys. Rev. Lett. **107**(4), 045901 (2011).
11. J. Ginn, B. Lail, J. Alda, and G. Boreman, "Planar infrared binary phase reflectarray," Opt. Lett. **33**(8), 779–781 (2008).
12. S. L. Wadsworth, P. G. Clem, E. D. Branson, and G. D. Boreman, "Broadband circularly-polarized infrared emission from multilayer metamaterials," Opt. Mater. Express **1**(3), 466–479 (2011).
13. C. L. Holloway, E. F. Kuester, J. A. Gordon, J. O'Hara, J. Booth, and D. R. Smith, "An overview of the theory and applications of metasurfaces: the two-dimensional equivalents of metamaterials," Ant. Propagat. Mag. **54**(2), 10–35 (2012).
14. Q. Feng, M. Pu, C. Hu, and X. Luo, "Engineering the dispersion of metamaterial surface for broadband infrared absorption," Opt. Lett. **37**(11), 2133–2135 (2012).
15. T. Zentgraf, J. Dorfmüller, C. Rockstuhl, C. Etrich, R. Vogelgesang, K. Kern, T. Pertsch, F. Lederer, and H. Giessen, "Amplitude- and phase-resolved optical near fields of split-ring-resonator-based metamaterials," Opt. Lett. **33**(8), 848–850 (2008).
16. P. Alonso-Gonzalez, M. Schnell, P. Sarriugarte, H. Sobhani, C. Wu, N. Arju, A. Khanikaev, F. Golmar, P. Albella, L. Arzubiaga, F. Casanova, L. E. Hueso, P. Nordlander, G. Shvets, and R. Hillenbrand, "Real-space mapping of Fano interference in plasmonic metamolecules," Nano Lett. **11**(9), 3922–3926 (2011).
17. E. C. Kinzel, J. C. Ginn, R. L. Olmon, D. J. Shelton, B. A. Lail, I. Brener, M. B. Sinclair, M. B. Raschke, and G. D. Boreman, "Phase resolved near-field mode imaging for the design of frequency-selective surfaces," Opt. Express **20**(11), 11986–11993 (2012).
18. M. Schnell, A. Garcia-Extarri, A. J. Huber, K. Crozier, J. Aizpurua, and R. Hillenbrand, "Controlling the near-field oscillations of loaded plasmonic nanoantennas," Nat. Photonics **3**(5), 287–291 (2009).
19. R. L. Olmon, M. Rang, P. M. Krenz, B. A. Lail, L. V. Saraf, G. D. Boreman, and M. B. Raschke, "Determination of electric-field, magnetic-field, and electric-current distributions of infrared optical antennas: a near-field optical vector network analyzer," Phys. Rev. Lett. **105**(16), 167403 (2010).
20. P. M. Krenz, R. L. Olmon, B. A. Lail, M. B. Raschke, and G. D. Boreman, "Near-field measurement of infrared coplanar strip transmission line attenuation and propagation constants," Opt. Express **18**(21), 21678–21686 (2010).
21. M. Schnell, P. Alonso-Gonzalez, L. Arzubiaga, F. Casanova, L. E. Hueso, A. Chuvilin, and R. Hillenbrand, "Nanofocusing of mid-infrared energy with tapered transmission lines," Nat. Photonics **5**(5), 283–287 (2011).
22. R. L. Olmon, P. M. Krenz, A. C. Jones, G. D. Boreman, and M. B. Raschke, "Near-field imaging of optical antenna modes in the mid-infrared," Opt. Express **16**(25), 20295–20305 (2008).
23. R. L. Olmon, H. A. Bechtel, M. C. Martin, and M. B. Raschke, (in preparation).
24. H. A. Bechtel, M. C. Martin, T. E. May, and P. Lerch, "Improved spatial resolution for reflection mode infrared microscopy," Rev. Sci. Instrum. **80**(12), 126106 (2009).
25. F. Huth, A. Govyadinov, S. Amarie, W. Nuansing, F. Keilmann, and R. Hillenbrand, "Nano-FTIR absorption spectroscopy of molecular fingerprints at 20 nm spatial resolution," Nano Lett. **12**(8), 3973–3978 (2012).
26. X. G. Xu and M. B. Raschke, "Near-field infrared vibrational dynamics and tip-enhanced decoherence," Nano Lett. **13**(4), 1588–1595 (2013).

1. Introduction

Optical metamaterials are obtained by engineering size, shape, and electronic confinement to achieve electromagnetic properties not native to the material, or even properties not typically found in nature. Manipulation of spectral properties [1–5] and phase control [6–8] is often achieved through frequency selective surface designs borrowed from radio technology and scaled to resonance with infrared wavelengths [9–12]. Recently, the term *metasurface* has been used to describe metamaterials consisting of a thin layer of elements with periodicity in two dimensions [8, 13, 14]. Here, electronic coupling between neighboring loops is used to mimic an ideal absorbing sheet, limiting optical dispersion and allowing broad-band absorbance.

The desired functionality of the metasurfaces relies on the local near-field interactions at deep sub-wavelength dimensions. In this work we utilize both broad-band synchrotron based and narrow-band laser based infrared scattering-scanning near-field optical microscopy (*s*-SNOM) in combination with far-field FTIR microscopy and theoretical simulations to investigate the spectral and spatial near-field mode characteristics of a specific metasurface design. This work builds on the previous successful demonstration of the use of *s*-SNOM for the investigation of metamaterial-type structures at infrared wavelengths [15–17], optical antennas [18, 19], and transmission lines [20, 21], yet represents the first application of a broad-band IR source for such investigations.

#188776 - $15.00 USD Received 16 Apr 2013; revised 2 Jul 2013; accepted 4 Jul 2013; published 11 Jul 2013

Near-field measurements using *s*-SNOM operating in mid-infrared (mid-IR) were made on metasurfaces consisting of square loop arrays. Three dimensional finite element methods are used to identify the resonant energy conditions and Eigen-modes within the antenna array. The arrays are designed to have an absorptive fundamental resonance in the range 8-22 μm. Far-field reflectance infrared spectroscopy (FTIR) resolves a strong absorption at the fundamental resonance as well as weaker higher order modes. Interferometrically detected narrow-band *s*-SNOM resolves the phase and magnitude of the evanescent near-field signal of both dipolar and quadrupolar resonant modes. Synchrotron based, broad-band *s*-SNOM reveals the standing wave patterns of the fundamental absorption mode and dielectric contrast due to the constituent materials.

2. Metasurface design and fabrication

The dimensionality of the square loop arrays was designed using finite element method software to set the fundamental absorption energy of the arrays. Simulations were run in Ansoft HFSS, a full wave electromagnetic solver, using the Floquet port method. This method allows for computation of the amplitude and phase of the local electric field as well as the far-field spectral properties. Each of the samples was designed with resonances at 60° incidence angle relative to surface normal with s-polarized light (transverse electric field) in order to improve the near-field response measurable by *s*-SNOM. Metasurfaces were constructed using either aluminum or gold square loops over an aluminum or chromium ground plane, separated by a BCB or ZnS dielectric standoff layer. Here, the Al / BCB / Al metasurface is presented as a more practical design (inexpensive and easy to fabricate) while the Cr / ZnS / Au metasurface is presented as an alternative design to avoid the loss bands in the dielectric layer. BCB is a commonly used infrared dielectric material due to its low cost fabrication by spin coating and relatively low loss over certain portions of the infrared spectrum. ZnS is used as an essentially lossless infrared material. A Cr ground plane was used in the ZnS design because it was found that ZnS adheres very well to it. The frequency dependent optical constants of the materials used in the design were determined via ellipsometry and employed in the simulation. Through successive parametric iterations of the geometrical factors in the design (such as size of the loop, line width, periodicity, and thickness of the dielectric layer) the 60° off-normal absorptivity was maximized.

The goal for Al loop design optimization was to create two metasurfaces which would exhibit a dipolar and quadrupolar resonance under the illumination conditions of the narrow-band *s*-SNOM apparatus. Simulations of the absorptivity at 10.6 μm under 60° incidence angle are shown in Fig. 1 with respect to the length of the square loop edge. This clearly shows strong resonant conditions when the loop edge is 2.0 and 3.75 μm, with the former being nearly unity absorptivity. By observing the near-fields in the simulation, it is clear that the 2.0 μm loops display a fundamental (dipolar) mode while the 3.75 μm loops displayed a harmonic (quadrupolar) mode at 10.6 μm and 60° incidence angle. Further investigation showed that the fundamental resonance of the 3.75 μm loops exists for an excitation wavelength near 22 μm.

The Al square loop samples were fabricated according to these optimized designs. First, an optically thick ground plane was deposited by resistive evaporation upon a clean Si wafer. Then, a BCB layer of 1.2 μm thickness was deposited via spin coating and curing in an inert environment. The loop elements were created by electron beam lithography followed by metallization and liftoff. The Al elements had a line width of 250 nm, line thickness of 75 nm, and periodicity of 5 μm. A composite SEM image of the fabricated structures is shown in Figs. 2(a) and 2(b).

#188776 - $15.00 USD Received 16 Apr 2013; revised 2 Jul 2013; accepted 4 Jul 2013; published 11 Jul 2013

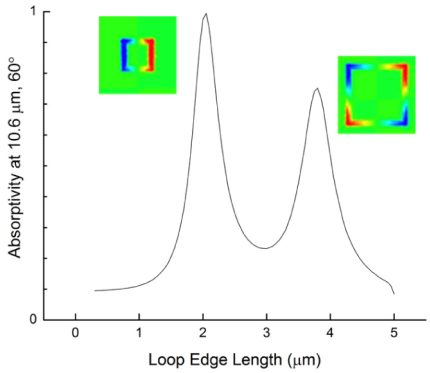

Fig. 1. Simulated absorptivity at 10.6 μm and 60° angle of incidence as a function of the loop edge length for the Al square loop designs. Unit cell schematics depicting the simulated near-field of the resonant cases at 2.0 μm and 3.75 μm are shown near their respective peaks for clarity. Near-field analysis shows that the 2.0 μm loops display a dipolar resonance while the 3.75 μm loops display a quadrupolar resonance.

Gold square loops were prepared in a similar manner using electron beam lithography. These samples utilize a Cr ground plane covered with a 215 nm ZnS spacer layer. Two gold samples were designed and fabricated with an edge length of 1.43 μm and periodicity of 1.79 μm and 5.79 μm. At 60° incident angle, finite element methods predict the tightly packed Au loops to be resonant near 9.5 μm and the loosely packed Au loops to be resonant near 8.7 μm, resulting from the change in coupling of the evanescent electric fields as a function of loop spacing. Additionally, the closely spaced loops form a highly resonant metasurface while the loosely spaced loops are much less resonant. SEM micrographs of the gold loop arrays are shown in Figs. 2(d) and 2(e).

3. Far-field Infrared Spectroscopy

Resonance conditions were identified at normal incidence in the far-field using reflectance geometry FTIR spectroscopy. Far-field spectra were collected using an infrared microscope in reflectance geometry with an unpolarized globar (50 μm aperture, 32x objective, N.A. 0.65, 18-40.5° angle of focus). The normal incidence simulated and experimental far-field absorptivity spectra [Figs. 2(c) and 2(f)] show broad resonances at 9.5 μm (small Al loops), 22 μm (large Al loops) 10 μm (tightly spaced Au loops) and 9.2 μm (loosely spaced Au loops). In general, the simulations show good agreement with the experimental absorptivity near the design wavelength of each metasurface. One possible exception to this is in the case of the large Al loops which are fundamentally resonant in the far-infrared. Here, it is unclear whether the discrepancy is real or simply due to poor signal quality of the FTIR at such long wavelengths. Somewhat marginal agreement between the simulated and experimental results is seen at wavelengths much shorter than that of the intended designs. This is likely due to the simulations assuming a high degree of spatial and temporal coherence that is not present in the FTIR experiment.

In all cases, the normal incidence resonances are observed to be shifted spectrally from the original finite element method designs, which were optimized for illumination at 60° angle of incidence. The Au/ZnS samples have resonance that is blue-shifted with increasing angle of incidence while the Al/BCB samples have a resonance that is red-shifted. (The latter is due to the presence of vibrational modes in the BCB polymer). The finite element method calculations showing the shifting of resonant absorptivity peaks with increasing angle of incidence qualitatively match the observed far-field spectral shifts observed at near-normal incidence.

#188776 - $15.00 USD Received 16 Apr 2013; revised 2 Jul 2013; accepted 4 Jul 2013; published 11 Jul 2013

The spectra for the Al samples on BCB spacer display a series of sharp peaks in the region 3-13 μm where higher order absorption modes are expected [Fig. 2(c)]. These sharp peaks are due to molecular vibrational modes in the BCB organic spacer layer. Optical constants derived from ellipsometry show major absorption bands in BCB at 9.5 μm, 12 μm, and 12.4 μm; the substrate absorptivity shown in Fig. 2(c) is intended to highlight the BCB absorptivity that is present in all data sets. Antenna-mode near-field enhancement of BCB stretching modes results in non-linear scaling of these peaks and prevents accurate background subtraction. Surface enhancement of vibrational modes can occur near resonant conditions of a plasmonic antenna. This is dependent upon both the spectral overlap of the plasmon resonance with the molecular vibration as well as the orientation and distance of the vibrational mode with respect to the evanescent electric fields of the antenna. Plasmon enhanced infrared absorption of the molecular vibrational modes is observed in energy corresponding to the fundamental absorption mode and above. Similar enhancement is observed for the large Al loops, though it is observed at an energy 2-4 times that of the fundamental absorption mode of the metasurface. We attribute this to the higher order optical modes in the metasurface.

Higher order resonances are also investigated for the gold samples. The broad transmission window of the ZnS spacer allows more accurate measurement of the metasurface resonance with less background interference. A sharp fundamental absorbance peak is observed at 10 μm in the tightly packed Au loops [Fig. 2(f)]. Up to three higher order modes of this resonance may be observed with smaller peaks occurring at 4.8 μm, 3.2 μm and 2.1 μm. The resonance conditions at 3.2 μ and 2.1 μm are predicted in simulation, while the peak observed near 4.8 μm is not. Due to decreased inter-element coupling, the loosely packed Au loops have a weaker fundamental absorbance at 9.2 μm, with a large higher order resonance observed near 2.5 μm. Both the fundamental resonance and higher order feature observed for the loosely packed Au loops are predicted in the simulation.

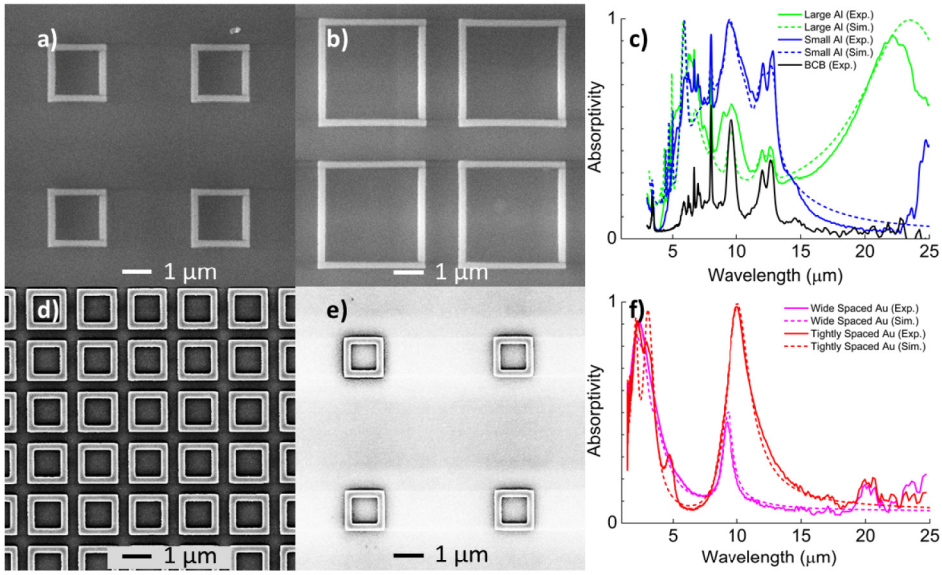

Fig. 2. SEM images of the fabricated metasurfaces (a) small Al square loop metasurface, (b) large Al loop metasurface, (d) tightly spaced gold loop metasurface with 1.79 μm periodicity (e) widely spaced gold loops with 5.79 μm periodicity. Experimental and simulated absorptivity, Al loop arrays as well as the BCB substrate (c) and Au loop arrays (f).

#188776 - $15.00 USD Received 16 Apr 2013; revised 2 Jul 2013; accepted 4 Jul 2013; published 11 Jul 2013

4. Near-field methods

Geometric confinement and local phase of resonant electric fields in a metasurface are resolved using *s*-SNOM. We measure the near-field response using both monochromatic laser based and broad-band synchrotron based *s*-SNOM.

Narrow-band *s*-SNOM utilizes a CO_2 laser source operating at 10.6 μm; the interferometric homodyne signal is detected by a Mercury Cadmium Telluride (MCT) detector as described previously [22]. In the current configuration, the reference arm of the interferometer contains a quarter waveplate, which rotates the interfering light to have opposite polarization as the incident beam. In this way, s-polarized light is used for resonant excitation of the metasurface, and the predominately p-polarized light collected from the tip interferes with p-polarized light from the reference arm. For each region of interest, scans are taken at several different mirror positions to interfere different phases of the reference arm. Phase and amplitude images determined by a least squares fit can then be represented as images of the evanescent electric field as a function of position on the sample.

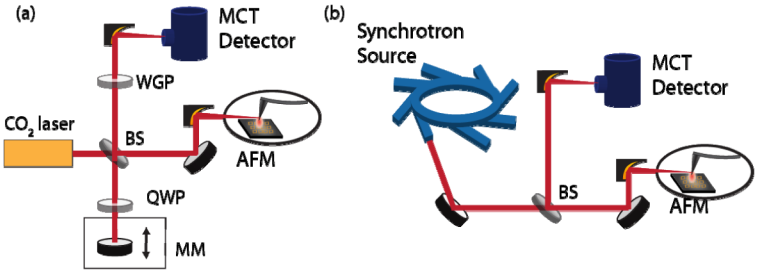

Fig. 3. Schematic of (a) monochromatic *s*-SNOM with a CO_2 laser source. The reference arm contains a moving mirror (MM) and quarter waveplate to allow interferometric detection with s- and p-polarized light. A wire grid polarizer (WGP) is also used to decrease background interference. Broadband synchrotron based *s*-SNOM (b) relies on a similar experimental setup. The reference arm is blocked during spatial imaging.

A broad-band *s*-SNOM was developed at beamline 5.4 of the Advanced Light Source, Lawrence Berkeley National Laboratory [23]. This source produces an ultra-broad-band infrared beam spanning the entire infrared region, limited by the BaF_2 beamsplitter and MCT detector to approximately the region 1.7-12.5 μm. This light is collimated to a 1.5 cm diameter beam and focused on an AFM tip using a custom parabolic mirror (NA ~0.4) with an effective focal length of 19.5 mm, resulting in a near diffraction-limited beam waist of 20 μm [24]. The focused synchrotron beam is incident on the AFM tip at an angle of 63.5° from normal incidence. Both s-polarized and p-polarized light, achieved by a periscope rotation of the beam, were used in this investigation. Polarization is maintained at the sample by aligning the incident beam parallel to the AFM cantilever (Arrow NC, f_o = 285 kHz). The near-field signal is demodulated with a lock-in amplifier (Zurich Instruments), and high contrast images were obtained at the first through third demodulations of the tip oscillation. An average beam power of 600 μW was found to produce large signal and allow detection with a fast time constant (1 –10 ms typical) and short imaging times.

Nano-FTIR is achieved by interferometric detection of the scattered signal, utilizing the movable mirror in a commercial FTIR [25]. An asymmetric interferogram is measured as a function of reference arm delay, resulting from the vibrational free induction decay [26]. Due to the long signal collection times for nano-FTIR spectroscopy, fully resolved phase and frequency images cannot be obtained. Instead, broad-band imaging of the evanescent fields is achieved by blocking the reference arm and collecting signal from either the full or limited spectral range. Self-homodyne detection amplifies the near-field signal through mixing with far-field scattered light. Although this technique mixes in phase and out of phase components of the near-field signal, signal collection is dramatically simplified for broad-band sources. In

#188776 - $15.00 USD Received 16 Apr 2013; revised 2 Jul 2013; accepted 4 Jul 2013; published 11 Jul 2013

general it is found that phase contamination in self-homodyne amplification occurs with large area scans on the order of the wavelength of light and becomes less important with small area scans and long incident wavelengths. In this study, we have observed constant phase of the self-homodyne reference within a single image across the range of image sizes (1-10 μm) examined, resulting in constant signal intensity across the imaging region.

5. Near-field results: Narrow-Band

Narrow-band *s*-SNOM was used to investigate the resonant near-field response of the optical metasurfaces with 10.6 μm illumination. Measured amplitude and phase of the electric field for the small loop metasurfaces [Figs. 4(a) and 4(c)] reveal a strong resonant signal above the dielectric contrast. The near-field imaging results agree qualitatively with the finite element simulations of amplitude and phase [Figs. 4(b) and 4(d)]. The *s*-SNOM amplitude signal has been normalized for comparison with the simulation. Measured and simulated amplitude data [Figs. 4(a) and 4(b)] show the familiar symmetric dipole type field amplitude pattern, with strong field on either side of the loop and a null across the horizontal edges. This is indicative of the fundamental mode of the structure. The field amplitude appears greater in the upper portions of the square loops as compared to the lower portions; this is attributed to the light source being located above the top of the image with the AFM tip shadowing each loop. The experimental and theoretical phase images [Figs. 4(c) and 4(d)] show characteristic evidence of an anti-symmetric dipole in the near-field signal. Some discrepancy is observed between theory and experiment here because the phase wrapping routines do not discriminate + π from -π well, and small errors near ± π appear as a sign flip. Accounting for sensitivity near π, the phase images are found to agree well with the predicted lowest order anti-symmetric dipole mode.

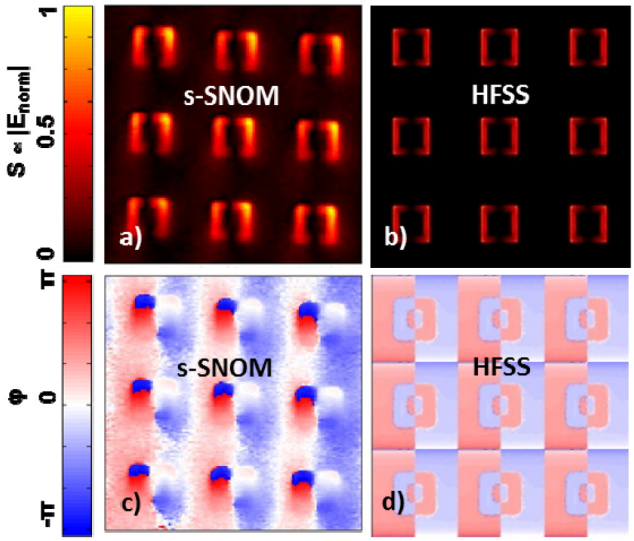

Fig. 4. Images of *s*-SNOM data and HFSS simulations for the small loop metasurface showing the normalized *s*-SNOM amplitude (a) and relative phase (c), as compared to the normalized electric field amplitude (b) and relative phase (d) values simulated in HFSS.

The measured and simulated near-field amplitude and phase results for the large loop metasurface are shown in Figs. 5(a)-5(d). The large loop Al square loops are investigated using the same 10.6 μm CO_2 laser, such that the laser is approximately resonant with twice the frequency of the fundamental absorption mode at 22 μm. As shown in the experimental and simulated amplitude section of the Figs. 5(a) and 5(b), respectively, the larger loops have strong amplitude at the corners with nulls at the center of each edge. Amplitude and phase are

#188776 - $15.00 USD Received 16 Apr 2013; revised 2 Jul 2013; accepted 4 Jul 2013; published 11 Jul 2013

both observed to have two orthogonal modes, with symmetric and anti-symmetric signals respectively, indicating observation of the second order quadrupole mode. The experimental phase image [Fig. 5(c)] appears to have a better qualitative match to the simulation [Fig. 5(d)] here as compared to that of the smaller loops, though the tip shadowing effect is still observed. Simulations show that this quadrupole mode exists only under excitation at angles of incidence greater than 40° from normal. At normal incidence, a weak dipole mode is seen in simulation. This mode at normal incidence could be predicted from the far-field reflectance FTIR spectra; however, large plasmon enhancement of molecular vibrations in the spacer layer restricts the ability resolve the peak of interest clearly. In this case, the *s*-SNOM is thus shown to be a more sensitive probe of resonant modes as compared to standard far-field measurements.

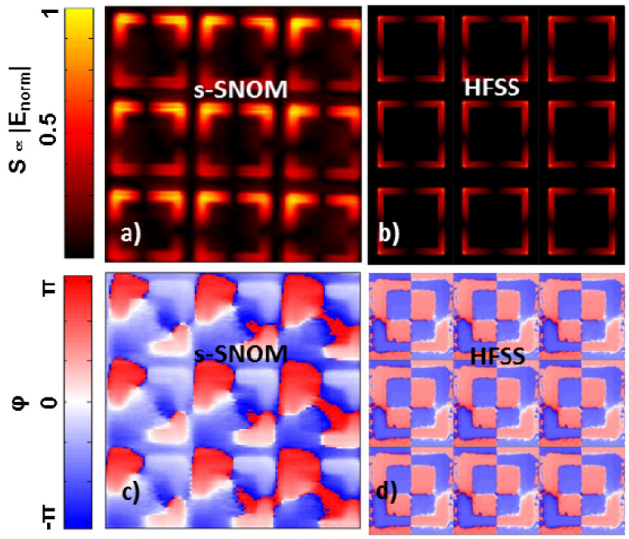

Fig. 5. Images of *s*-SNOM data and HFSS simulations for the large loop metasurface showing the normalized *s*-SNOM amplitude (a) and relative phase (c), as compared to the normalized electric field amplitude (b) and relative phase (d) values simulated in HFSS.

6. Near-field results: Broad-Band

Both in plane and out of plane electric field resonance are examined using the broad-band synchrotron source. The out of plane resonance, achieved using p-polarized incident light, results in higher signal strength due to antenna amplification parallel to the tip axis. Topography as well as first and second harmonic demodulations of the optical signal are simultaneously measured in the small Al square loops [Figs. 6(a)-6(d)]. Spatial resolution in this image is found to be near tip-limited, as the optical intensity matches the topography at the loop edge nearly perfectly. The square loops show a significant evanescent near-field contribution above the non-resonant dielectric contrast [Figs. 6(b)-6(d)]. It is perhaps surprising that relatively narrow-band resonant absorption by the metasurface is readily detectable above the expected dielectric contrast using a detection method that is not frequency resolved. This supports the presence of highly absorbing or emitting modes in the metasurface, in good agreement with far-field spectra.

Broad-band imaging of the near-field signal in Al square loops reveal a dipole mode parallel to the axis of incident light. The highest electric field strengths are observed near the top and bottom edges of the square loop, with a clear node existing through the middle of the loop. The anti-symmetric signal, with a single nodal plane running through the square loop array, is in close agreement with phase images observed in narrow-band *s*-SNOM.

#188776 - $15.00 USD Received 16 Apr 2013; revised 2 Jul 2013; accepted 4 Jul 2013; published 11 Jul 2013

Constructive and destructive interference are observed in the optical signal from the metasurface as a result of interference with the self-homodyne reference scattering signal. Self-homodyne detection does not directly distinguish phase from amplitude in the optical signal: the observed anti-symmetric images indicate a dominant contribution from phase of the electric field. The anti-symmetric signal appears most strongly in the first harmonic demodulation, with a decreasing negative portion of the optical signal at higher harmonics. The near-field dielectric contrast also increases with increasing lock-in demodulation, and an apparent decrease in the relative strength of the resonant signal at higher demodulations may result from a larger relative enhancement of dielectric contrast.

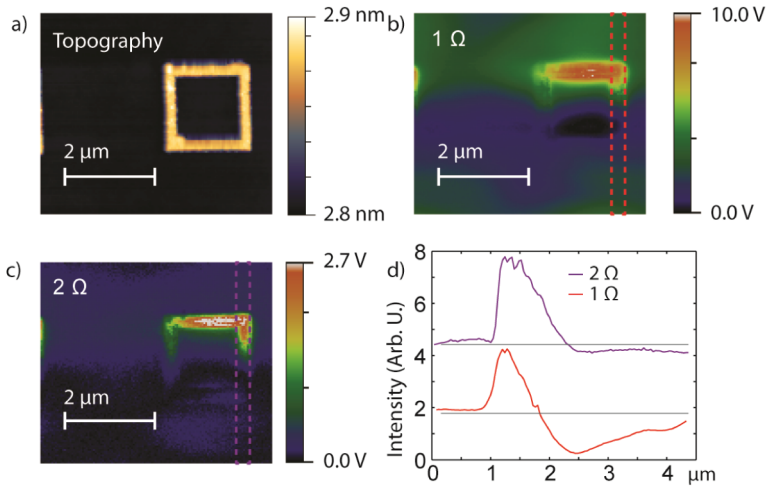

Fig. 6. Synchrotron based infrared *s*-SNOM of small aluminum loops using p-polarized light showing topography (a), lock-in demodulations 1 Ω and 2 Ω (b) and (c), and line cuts of the intensity (d). Here, Ω denotes the harmonic of the demodulation, such that 2 Ω refers to the second harmonic.

Investigation of the near-field signal parallel to the metasurface plane was carried out using s-polarized light. Figures 7(b)-7(d) show s-polarized broad-band excitation and detection on the Au array resonant with 1.79 µm periodicity. The signal with s-polarized light was found to be significantly smaller in general, as the geometry of the tip favors p-polarization for both incident light and detection. Images resulting from the in plane component of the near-field are nearly identical to the out of plane p-polarized light. Further, neither the change in spacer material between BCB and ZnS nor the change in metal is found to influence the near-field signal. The nearly identical near-field signal from the Au and Al metasurfaces supports the fundamental assumption that conductivity and geometry, rather than details of material properties, define the response of the resonant modes.

The intensity shown for the s-polarized incident light, [Figs. 7(b)-7(d)] is spatially inverted compared to the p-polarized condition. The sign of the near-field dipole resonance flips dependent upon the phase of the scattered self-homodyne reference signal: image intensity inverts with a phase shift of 180° in the reference signal. Because the samples possess square symmetry, and the electric field is coupled to the tip perpendicular to the sample, dipole resonance can also occur parallel, anti-parallel, or orthogonal to the incident light. The direction of the near-field dipole is thus highly sensitive to the details of the alignment, tip-sample coupling, and the local phase of the reference field.

#188776 - $15.00 USD Received 16 Apr 2013; revised 2 Jul 2013; accepted 4 Jul 2013; published 11 Jul 2013

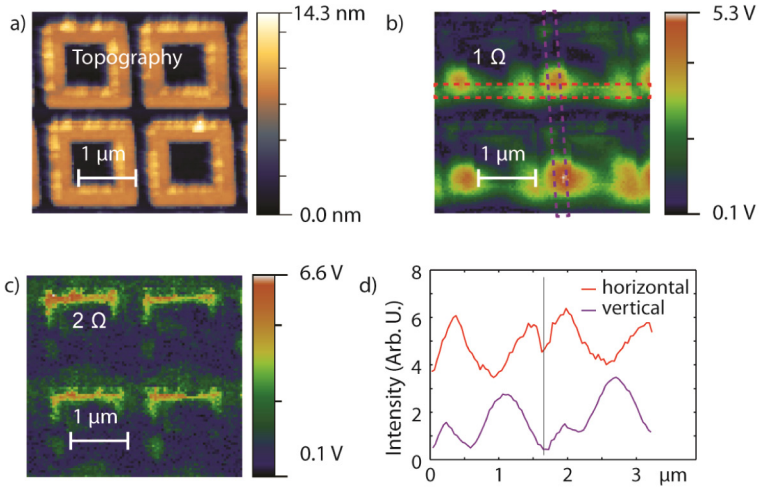

Fig. 7. Synchrotron based infrared *s*-SNOM of gold loops with 1.79 µm periodicity with s-polarized light showing topography (a), lock-in demodulations 1 and 2 (b) and (c), and line cuts of the intensity (d). An anti-symmetric dipole response is observed in the vertical line cut along the gold loops, while a symmetric response is resolve in the horizontal line cut.

The presence of quadrupole and higher order modes was investigated in three samples with fundamental resonance near 10 µm. Because the broad-band source spans the excitation region 1.7-12.5 µm, higher order modes may be excited within the metasurface. The dipole mode corresponding to the fundamental absorption is found to point parallel or antiparallel to the Poynting vector of the incident light. The phase of the electric field is found to dominate the observed near-field signal in the vertical direction for both s- and p-polarized incident light. Little spatial variation was observed along the beams of the square loop using p-polarized light, as could be expected for a dipole mode. Using s-polarized light, however, the beams show a strong symmetric optical response [Fig. 7(d)]. This may result from an excitation by higher order modes, resulting in a symmetric signal. More likely, symmetric response along a horizontal beam results from the symmetric amplitude signal, which is simultaneously amplified. These data suggest, however, that nodes exist in both the horizontal and vertical directions within the same image, which would support the presence of a quadrupole mode. A quadrupole may also exist simultaneously with the dipole mode while remaining undetected due to a lower signal strength in the higher mode. Frequency resolved interferometric detection will be required in future studies to clearly identify the role of higher order resonant modes.

7. Conclusion

Square loop based metasurfaces were fabricated with gold or aluminum loops above a molecular or ZnS spacer layer and metallic ground plane. Far-field reflectance FTIR revealed clear fundamental resonances closely matching the theoretical modeling from finite element method analysis. The Au/ZnS arrays revealed weak absorptions from higher order resonance modes, while the Al/BCB metasurface showed antenna enhancement of the BCB molecular vibrations near the expected higher modes. Near-field imaging using *s*-SNOM showed that the electric field in the direction normal to the sample displays strong multipolar resonances. Monochromatic excitation at 10.6 µm was found to resonantly couple to both dipolar and quadrupolar modes. This is evidenced in both the electric field amplitude and phase images. Broad-band *s*-SNOM of the metasurface, however, found that the dominant contribution resulted from the lowest order dipole mode. Our results show that infrared *s*-SNOM is a powerful technique for imaging the electric fields resonant within metasurfaces.

#188776 - $15.00 USD Received 16 Apr 2013; revised 2 Jul 2013; accepted 4 Jul 2013; published 11 Jul 2013

Acknowledgments

A portion of this research was supported by the Laboratory Directed Research and Development program at Sandia National Laboratories. Sandia is a multi-program laboratory operated by Sandia Corporation, a Lockheed Martin Company, for the U.S. Department of Energy under contract DE-AC04-94AL85000. The Advanced Light Source is supported by the Director, Office of Science, Office of Basic Energy Sciences, of the U.S. Department of Energy under Contract No. DE-AC02-05CH11231. Funding from the National Science Foundation (NSF CAREER grant CHE 0748226, NSF grant 1204993, and NSF grant 1068050) is gratefully acknowledged. JD gratefully acknowledges support from the SMART Scholarship, funded by OSD-T&E (Office of Secretary Defense-Test and Evaluation), Defense –Wide / PE0601120D8Z National Defense Education Program (NDEP) / BA-1, Basic Research.

#188776 - $15.00 USD Received 16 Apr 2013; revised 2 Jul 2013; accepted 4 Jul 2013; published 11 Jul 2013